GPU-accelerated Multi-sensor 3D Mapping for Remote Control of Mobile Robots using Virtual Reality

Sebastian P. Kleinschmidt and Bernardo Wagner
Institute of Systems Engineering - Real Time Systems Group, Leibniz Universität Hannover,
Appelstr. 9A, D-30167, Hannover, Germany

Keywords: Virtual Environments, Augumented Reality, Sensorfusion, GPU-acceleration.

Abstract: In this paper, a new virtual reality (VR) control concept for operating robots in search and rescue (SAR) scenarios is introduced. The presented approach intuitively provides different sensor signals as RGB, thermal and active infrared images by projecting them onto 3D structures generated by a Time of Flight (ToF)-based depth camera. The multichannel 3D data are displayed using an Oculus Rift head-up-display providing additional head tracking information. The usage of 3D structures can improve the perception of scale and depth by providing stereoscopic images which cannot be generated for stand-alone 2D images.

Besides the described operating concept, the main contributions of this paper are the introduction of an hybrid calibration pattern for multi-sensor calibration and a high performance 2D-to-3D mapping procedure. To ensure low latencies, all steps of the algorithm are performed parallelly on a graphics processing unit (GPU) which reduces the traditional processing time on a central processing unit (CPU) by 80.03%. Furthermore, different input images are merged according to their importance for the operator to create a multi-sensor point cloud.

1 INTRODUCTION

Mobile robots are increasingly used in situations, where humans cannot operate without placing themselves in danger. In typical search and rescue (SAR) scenarios, time is mission critical and can make the difference between a victim's life or death. Therefore, it is important to work as time-efficient as possible. At disaster sites, the immediate availability of trained rescue forces cannot be guaranteed. Often, skilled manpower arrives only hours or days after the incident. In most cases, nearby but untrained or less qualified people arrive at the disaster site first.

This paper presents a robot operating concept, which significantly reduces the qualification needed to operate a robot at disaster sites by providing an intuitive, three-dimensional virtual reality (VR)-based interface. This interface merges two-dimensional sensor data such as RGB, thermal and active infrared images with three-dimensional information generated by a Time of Flight (ToF)-based depth sensor. The merged information is used to generate a three-dimensional, multichannel point cloud which is then visualized via a head-mounted display including head-tracking to ease the perception of depth and scale. Thus, it is possible to get a better overview of the disaster site. The operator can switch between the different channels of the generated point cloud to display the information needed in the current situation (e.g. thermal imaging for buried victims identification or active infrared based night vision for operating in darkness). By combining the different information of RGB, IR and thermal imaging, it is possible to get the necessary information according to the priority task defined (such as finding covert persons) without manually switching between the channels. Figure 1 shows a victim highlighted based on the thermal image which is mapped on a depth image.

High latency is the main reason for simulator sickness (LaValle et al., 2014). Therefore, one major contribution of this paper is the reduction of latency by performing the whole mapping procedure on a graphics processing unit (GPU). As a result, the approach may help to reduce fatigue during operation thus extending the possible operation time a single operator may achieve.

The rest of this paper is organized as follows: Section 2 gives an overview of related scientific work in the area of remote controlled robots and image-to-depth projection. Then, the approach for multi-sensor depth mapping is presented, including intrinsic and extrinsic calibration, filtering techniques and

Kleinschmidt, S. and Wagner, B.
GPU-accelerated Multi-sensor 3D Mapping for Remote Control of Mobile Robots using Virtual Reality.
DOI: 10.5220/0005692200190029
In *Proceedings of the 13th International Conference on Informatics in Control, Automation and Robotics (ICINCO 2016) - Volume 2*, pages 19-29
ISBN: 978-989-758-198-4

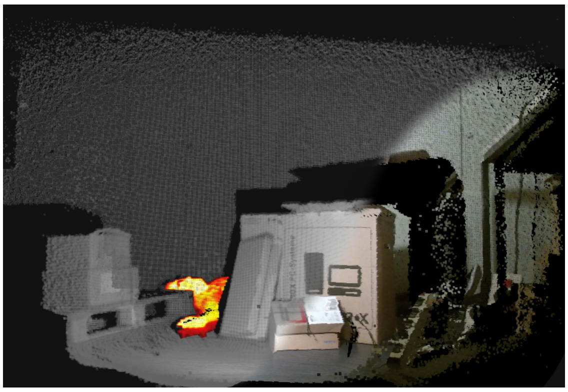

Figure 1: Multi-sensor 3D mapping can help rescue forces to get a better awareness of the situation.

the mathematical background for 2D-to-3D projection. Following, the full parallel implementation of the algorithm is described. Section 4 provides a practical implementation of the described approach and presents results of the mapping process. The paper ends with an evaluation of the shown method followed by a final conclusion and an outlook on further work.

2 RELATED WORK

Besides operating robots in SAR scenarios, teleoperation is used in varying applications (Cui et al., 2003) such as space (Stoll et al., 2009), undersea (Ridao et al., 2007) or medical robotics. Simple teleoperating systems are based on monocular RGB cameras displayed on two-dimensional screens (Hainsworth, 2001). The operated robot is usually equipped with either a single camera or multiple ones (Hainsworth, 2001)(Okura et al., 2013) in order to increase the operator's field of view. For this reason, omnidirectional cameras are often used to enable the operator to change the view without causing a delay because the camera position has to be changed by actuators (Saitoh et al., 2006). In most applications, additional information such as sensor data are visualized in a graphical user interface (GUI) as an overlay or on additional displays (Hainsworth, 2001)(Nguyen et al., 2001).

For humans, moving the head is the natural way to explore the environment. The first teleoperation approaches using tracked head-mounted displays (HMD) were based on omnidirectional cameras to visualize 360° images. Looking at an omnidirectional camera image, the operator still gets only a two-dimensional impression of the robot environment with limited perception of depth and scale. Using monocular cameras, this disadvantage can be compensated by using structure from motion (SFM) techniques as done in (Saitoh et al., 2006). Besides the application of SFM, multi-camera systems (Yong et al., 1998) or depth cameras (Okura et al., 2013) are needed to provide full three-dimensional information to allow the perception of scale and depth.

The work presented in (Okura et al., 2013) describes a teleoperation interface enabling an operator to control a robot from freely configured viewpoints visualized by a head-mounted display and a head-tracker. For environmental perception, the robot is equipped with four structured light (SL)-based depth cameras. To avoid simulator sickness and to enable the operator to react fast enough on occurring events, all delays have to be kept as small as possible.

In contrast to the approach presented in this paper, the existing virtual reality concepts only use RGB-D information. Projecting two-dimensional information onto three-dimensional structures is useful in many areas such as entertainment, medical applications or the building sector. RGB-D mapping using depth cameras is state-of-the-art in robot applications as presented in (Henry et al., 2010), (Endres et al., 2013) and (Izadi et al., 2011). The works presented in (Vidas et al., 2013), (Vidas and Moghadam, 2013) and (Moghadam and Vidas, 2014) describe a hand-held device built out of a RGB-D and a thermal camera. The device is used for thermal-to-3D mapping which is helpful to monitor the energy efficiency of building structures. From the authors' perspective, the device has neither been implemented on a mobile robot, nor makes use of GPU-acceleration. Besides, a GPU suited implementation of the mapping procedure is necessary to provide mapped, three-dimensional structures to ensure low latency for virtual reality applications as presented in this paper. In contrast to existing approaches, the work presented in this paper uses multi-sensor data to create a merged point cloud, which selectively maps different image sources according to their importance to one output point cloud.

3 APPROACH

The following section describes the approach used in this paper to project two-dimensional images from different cameras onto three-dimensional structures which are finally visualized by a head-mounted display. This procedure includes the following steps:

1. **Preprocessing and Filtering:** The quality of the final multi-channel point cloud depends on the

quality of the depth image. Therefore, measurement noise and errors have to be filtered before mapping and thus appropriate filters have to be applied.

2. **Hybrid Calibration:** To perform mapping, it is necessary to determine the camera parameters to remove lens distortion. For the mapping process, the homogeneous transformation between the used sensor coordinate systems need to be known. Consequently, corresponding points have to be identified in the sensor images. As a result of varying working principles of the sensors (e.g. RGB and thermal), a special calibration pattern is necessary to identify corresponding points.
3. **Time Synchronization:** To reduce the mapping error based on time differences due to varying measurement rates, messages are filtered according to their time stamp.
4. **Parallel Mapping:** The pixels of the filtered and intrinsic calibrated depth image are used to generate a set of three-dimensional points, the two-dimensional images can be mapped on. Based on the performed extrinsic calibration, the point cloud is transformed into the coordinate system of the two-dimensional camera as preparation for the mapping. Then the image is projected onto the point cloud. Parallely, the mapping procedure is performed on the GPU.
5. **Selective Mapping:** The mapped point clouds are then merged to a single one, in which the most relevant information of all mapped input images are visualized. This step includes the highlighting of hidden persons by the thermal image and illuminating dark regions in the RGB image by the active infrared image.

Sections 3.1 to 3.6 are structured according to the presented order of steps.

3.1 Preprocessing

To increase the quality of the mapped three-dimensional model and to avoid mapping errors, it is important to preprocess the depth image which is typically affected by measurement noise and errors.

To prevent an error prone projection caused by image noise in the depth image, the depth image is filtered using a bilateral filter as described in (Tomasi and Manduchi, 1998). In contrast of a box, bilinear or Gaussian filter, by using a bilateral filter, the surfaces of the object are smoothed preserving edges at the same time due to an additional range component.

To remove single measuring errors appearing as outliers in the free space (therefore often referenced to as *flying pixels*), a threshold filter is applied based on the average distance of the surrounding pixels which are unequal to zero. The mean distance can be determined according to:

$$p(i,j) = \frac{1}{u}\sum_{l,m} ||f(i,j) - k(l,m)||^2 \qquad (1)$$

and

$$k(l,m) = \begin{cases} f(l,m), & \text{for } f(l,m) \neq 0 \\ f(i,j), & \text{else} \end{cases} , \qquad (2)$$

Where u is the number of surrounding pixels for that $k(l,m)$ is unequal to zero. With the threshold θ, the final value of the filtered depth image $depth(i,j)$ is given through:

$$g(i,j) = \begin{cases} f(i,j), & \text{for } p(i,j) < \theta \\ 0, & \text{else} \end{cases} . \qquad (3)$$

3.2 Hybrid Calibration

Like any other camera, depth, thermal or RGB cameras are affected by lens distortion and inaccuracies during production and therefore need to be intrinsically calibrated. Before sensor data can be projected, the cameras need to be extrinsically calibrated also. State-of-the-art calibration techniques for traditional two-dimensional cameras are presented in (Brown, 1971), (Zhang, 1999) and (Zhang, 2000). Considering that typical two-dimensional calibration patterns are unsuited for thermal and depth calibration, a hybrid calibration pattern is presented in this section, which enables multi-sensor to depth calibration for a variety of imaging techniques.

Regarding the different working principles of the used sensors, the calibration pattern used for the calibration of a specific camera varies. For the intrinsic calibration of a RGB camera, a typical printed black and white chessboard provides points in the pattern coordinate system which can be identified in the camera image. By using a strong infrared light source, the same pattern can be used to calibrate the active infrared camera. Since the temperature of a printed pattern is equally distributed over the pattern after all balancing processes are completed, it is not possible to identify the necessary amount of calibration points in the thermal image using a printed pattern. To solve this issue, heaters can be applied at dedicated positions in the calibration pattern coordinate systems to identify corresponding points for calibration purposes. In case of ToF cameras, the amplitude image (active infrared) can be used for intrinsic calibration based on the working principle of ToF. Besides using the infrared image, it is also possible to create a chessboard, where every square of the chessboard varies in height and thus providing points in the calibration pattern that can be identified by depth.

If the same calibration pattern is visible in two different camera images at the same time, the transformation between each camera and the chessboard can be used to compute the transformation between both camera coordinate systems. This requires, that at least $N = 3$ points of the pattern given in the chessboard coordinate system can be identified in both images at the same time.

According to this constraint, considering the different working principles of depth, IR, RGB and thermal cameras, a typical black and white calibration pattern is unsuited for an extrinsic calibration. For example, in the image of the thermal camera, the printed structure of the pattern would look uniform based on the same temperature and material of the chessboard and could not be identified. The remaining difference in the thermal image based on the different emissivity of the black and the white color is not sufficiently large for a calibration as needed for high accurate sensor mapping. A similar issue takes effect for the depth image, where corresponding points would look uniformly based on a similar depth.

To be able to identify at least three corresponding points in the camera images, a hybrid chessboard pattern needs to be designed, in which the black and the white squares differ in material, temperature and depth. If the depth camera can be calibrated using an intensity image as described in this section, the pattern does not need to vary regarding depth. For this purpose, the pattern needs to be built out of different materials as plastic and metal, whereas one color is heated to a constant temperature difference. The theoretical setup for such a calibration is shown in Figure 2.

Figure 2 shows a RGB and a thermal camera looking at a hybrid calibration pattern where every square of the chessboard distinguishes in color and temperature. The transitions between the chessboard squares can be identified in the RGB image because of the variation in color. In contrast, the transitions in the thermal image can be identified based on the variation in temperature caused by the heat pads attached to the background of the squares. To prevent the heat to spread through the pattern, the squares have to vary regarding their thermal conductivity to ensure clear temperature transitions in the thermal image.

The computed transformation between two cameras is limited in accuracy by the camera resolution and disturbance variables such as image noise. To decrease the error of the resulting transformation, the transformation is computed for an array of coincident images. To find the local minimum of the reprojection error for the transformation, the Levenberg-Marquardt iterative algorithm is used for optimization. The realization of the hybrid calibration pattern is presented in Section 4.2.

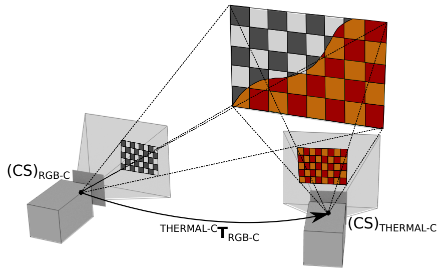

Figure 2: Heated calibration pattern for extrinsic calibration of RGB and thermal camera.

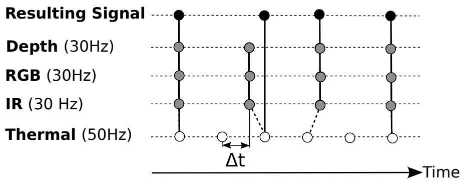

Figure 3: Synchronization of cameras working at asynchronous measurement rates.

3.3 Time Synchronization

Even if the sensors are synchronized regarding a global system time, measurement updates are typically occurring at different measurement rates. To reduce resulting mapping errors as they would occur when depth images are registered to data from a different time, the time difference has to be kept as small as possible.

Figure 3 shows four input signals at different measurement rates of 30 Hz and 50 Hz.

The depth, RGB and IR camera are working time-synchronized at $f_d = f_{RGB} = f_{IR} = 30\ Hz$, the measurement rate of the thermal camera differs with a measurement rate of $f_{th} = 50\ Hz$. The maximum time difference Δt_{max} between a depth, RGB or IR measurement and a thermal measurement is defined by the faster measurement rate of the thermal camera f_{th}:

$$\Delta t_{max} = \frac{1}{2 f_{th}} = 10\ ms. \qquad (4)$$

If Δt between two succeeding measurements is less or equal Δt_{max}, the messages are used for mapping. If $\Delta t > \Delta t_{max}$, the first measurement is discarded and the time measurement is repeated for the second measurement.

The resulting update rate for the synchronized signal f_{rs} varies according to Equation 5 and has an upper bound given by the measurement rate of the depth camera f_d.

$$f_d \geq f_{rs} \geq \frac{1}{\frac{1}{f_d}+\frac{1}{2f_{th}}}. \tag{5}$$

3.4 Mapping

The equation for projecting a point from the physical world into the camera image plane can be used to reconstruct a three-dimensional point ${}_{(d)}\mathbf{X}_p$ given ${}_{(I_d)}\mathbf{x}_p$, the associated point in the image plane in a filtered and intrinsic calibrated depth image (I_d) (see Section 3.1) by inverting $\mathbf{M}$ as shown in Equation 6.

$${}_{(d)}\mathbf{X}_p = {}_{(d)}\mathbf{M}^{-1}{}_{(I_d)}\tilde{\mathbf{x}}_p. \tag{6}$$

The two dimensional point ${}_{(I_d)}\tilde{\mathbf{x}}_p$ is given as homogeneous vector where ${}_{(I)}x_p$ and ${}_{(I)}y_p$ are the screen coordinates, starting in the upper left corner of the image.

$${}_{(I_d)}\tilde{\mathbf{x}}_p = \begin{bmatrix} {}_{(I_d)}x_p & {}_{(I_d)}y_p & {}_{(I_d)}w_p \end{bmatrix}^T, \tag{7}$$

where ${}_{(I_d)}w_p$ in ${}_{(I_d)}\tilde{\mathbf{x}}_p$ is given by the depth value in the depth image according to

$${}_{(I_d)}w_p = {}_{(d)}Z_p = d({}_{(I_d)}x_p, {}_{(I_d)}y_p)s_d. \tag{8}$$

The inverse ${}_{(d)}\mathbf{M}^{(-1)}$ can be computed as follows:

$${}_{(d)}\mathbf{M}^{(-1)} = \frac{1}{{}_{(d)}f_{x(d)}f_y} \begin{bmatrix} {}_{(d)}f_y & 0 & -{}_{(d)}c_{x(d)}f_y \\ 0 & {}_{(d)}f_x & -{}_{(d)}c_{y(d)}f_x \\ 0 & 0 & {}_{(d)}f_{x(d)}f_y \end{bmatrix}, \tag{9}$$

In Equation 8, s_d is the scale factor, which relates the depth value in the depth image to ${}_{(d)}Z_p$ the depth in the camera coordinate system of the depth camera.

Using Equations 6 to 8, the coordinates of a three-dimensional point in the depth camera's coordinate system can be computed for every two-dimensional point in screen coordinates of the depth image. By upscaling the depth image and therefore the quantity of pixels which can be registered to 3D points.

To perform a mapping between a calibrated two-dimensional image of a camera c and the generated set of three-dimensional points, every point given in the point cloud ${}_{(d)}\widetilde{\mathbf{X}}_p$ needs to be transformed into the coordinate system of the camera c. This can be done using the extrinsic calibration described in Section 3.2:

$${}_{(c)}\widetilde{\mathbf{X}}_p ={}^{c}\,\mathbf{T}_{d(d)}\widetilde{\mathbf{X}}_p. \tag{10}$$

To complete the mapping of a point ${}_{(c)}\widetilde{\mathbf{X}}_p$ given in the corresponding coordinate system of a two-dimensional camera, the point needs to be projected onto the image plane of the camera c.

$${}_{(I_c)}\tilde{\mathbf{x}}_p = {}_{(c)}\mathbf{M}_{(c)}\widetilde{\mathbf{X}}_p. \tag{11}$$

The color of the three dimensional point is given by the color of the image point ${}_{(I_c)}\mathbf{x}_p$. After merging the point cloud and the image source, the point cloud is retransformed to the depth camera coordinate system:

$${}_{(d)}\widetilde{\mathbf{X}}_p ={}^{d}\,\mathbf{T}_{c(c)}\widetilde{\mathbf{X}}_p. \tag{12}$$

3.5 Parallelization

The parallelized mapping procedure is presented in figure 4.

The mapping procedure is separated into code, which is executed on the CPU (*host*) and code which is executed in parallel on the GPU (*device*). Therefore, the data necessary to perform the computations for mapping need to be transferred between host and device memory to be processed. Because *host-to-device* and *device-to-host* copies are time consuming and increase computation time (compared to CPU based approaches, where all data already are on the device they are processed on), it is necessary to keep them to a minimal number.

For this reason, the extrinsic and intrinsic calibration parameters are transferred once during initialization and are kept in GPU memory. After time synchronization, corresponding data are loaded in the host memory. Before parallel processing, they are transferred to the device memory, which has been allocated during initialization. Because the resolution of the depth, RGB, IR and thermal image is known a priori, the size of the allocated memory is static. During runtime, multiple copies of the program can be executed in parallel on GPU *blocks*. Because every point of the point cloud can be independently computed based on the filtered depth image, the computation is performed in parallel on a fixed number of blocks given by the resolution of the depth image. According to Section 3.4, after point cloud generation, the points are transformed according to the extrinsic relation of the cameras and subsequently projected into the image plane. Because the amount of computations in these steps is high but the involved calculations are simple and are independent of each other, these steps are also well suited to be performed in parallel blocks on the GPU. After inverse transformation, the point cloud is written into the host memory for visualization. To optimize the mapping duration further, the practical implementation deviates

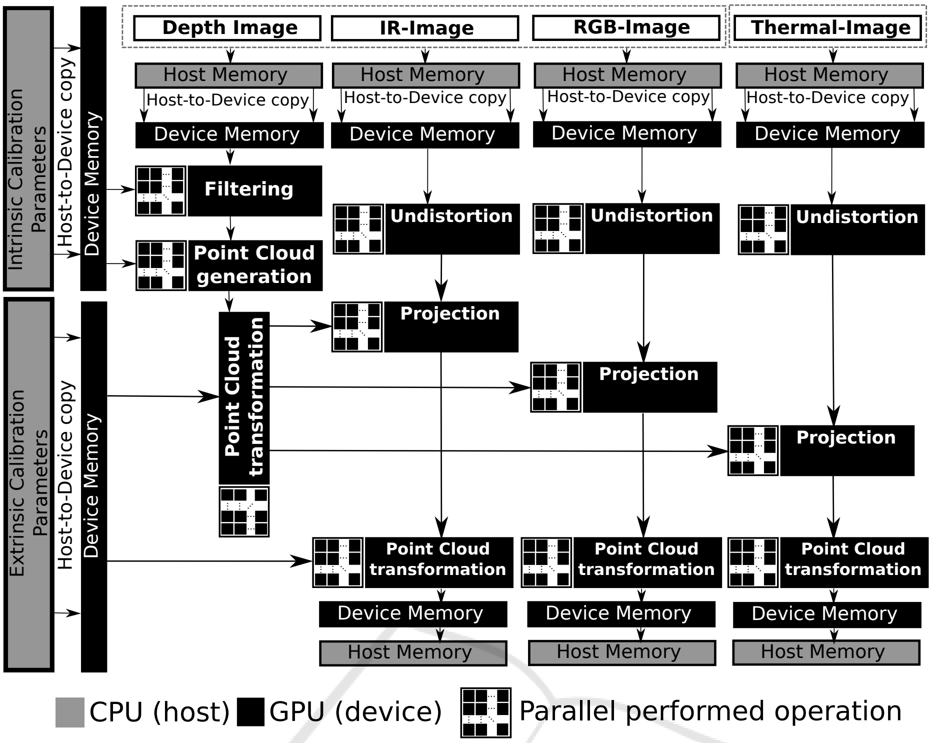

Figure 4: Overview of the software architecture.

from the procedure presented in figure 4 and is only performed for the selected output point cloud. Therefore, the number of host-to-device and device-to-host copies during runtime is decreased from 7, which are necessary to provide mapping for all point clouds, to 3. Excluded from this number are the host-to-device copies of the extrinsic and intrinsic calibration parameters, which have only to be performed once on start.

3.6 Selective Mapping

If all point clouds are selected for mapping in the previous step, a selective mapping procedure can be performed, which generated a point cloud, in which points are mapped according to their importance for the operator. The algorithm is presented in pseudocode below.

To avoid dark regions in the RGB image, dark points are replaced by the mapped IR points, if the brightness is below a given threshold. Subsequently, noticeable regions in the thermal image are mapped with priority to the point cloud, if they exceed a predefined threshold to highlight buried persons or hot regions which could be dangerous for the robot.

Algorithm 1: Selective Point Cloud Fusion.

```
Input: RGBD-, IRD-, THERMAL-Point Cloud
Output: Multi-Sensor Point Cloud
Initialize Output Point Cloud $P$
for each Point $p$ in Point Cloud $P$ do
    if $(\frac{R+G+B}{3}) < brightnessTresh$ then
        P = IR
    end if
    if $THERMAL > thermalTresh$ then
        P = THERMAL
    end if
end for
return $P$
```

4 EXPERIMENTS

The following section describes the experimental setup which is used to evaluate the results of Section 3.

4.1 Experimental Setup

For evaluation purposes, a *Pioneer 2* mobile robot has been equipped with a *FLIR A655sc* thermal camera (640 x 480 @ 50 fps) and a *Microsoft Kinect v2* depth-sensing camera providing RGB (1920 x 1080

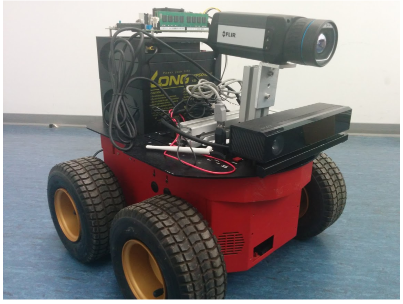

Figure 5: Pioneer 2 mobile robot equipped with a Microsoft Kinect v2 depth-sensing camera and a FLIR A655sc thermal camera.

@ 30 fps), depth (512 x 424 @ 30 fps) and active IR images (512 x 424 @ 30 fps). In contrast to the *Kinect 1*, which is based on structured light to estimate depth, the *Kinect 2* collects depth information based on ToF measurements. To enable extrinsic calibration, both cameras are rigidly mounted on the Pioneer as shown in Figure 5.

The sensor data are prompted and compressed onboard by a *KTQM87 mITX* board with an Intel quad core i7 CPU and 16 GB RAM running Ubuntu 14.04 64-bit. To power the Pioneer 2 and the connected sensors, the standard power supply is replaced with a 12 V 50 Ah car battery.

The compressed information is then transmitted via WiFi to a PC with an Intel quad core i5-4570 CPU, 16 GB RAM and a GeForce GTX 970 GPU. Subsequently, the data are preprocessed and registered according to Section 3. The resulting multi-channel point cloud is visualized using *RViz*. To render the stereo images for the Oculus Rift, the Oculus Rviz Plugin has been used[1]. The data are displayed to the operator using an *Oculus Rift Developer Kit 2* by *Oculus VR*. The head movement is tracked by the Oculus Rift and used to move the camera in Rviz. The operator can control the Pioneer 2 using a *Logitech Cordless Rumble Pad 2*.

Figure 6 gives an overview of the input and output structure used for the evaluation.

Besides, the intrinsic and extrinsic calibration which has only to be performed once, all parts of the presented method are programmed to work in parallel taking advantage of the GPU.

4.2 Intrinsic and Extrinsic Calibration

To be able to identify corresponding points for calibration in the RGB, IR, depth and in the thermal image as mentioned in Section 3.2, a hybrid chessboard pattern has been designed for calibration, in which the black and the white squares differ in color, depth, material and temperature. For this purpose, the black squares are made of metal, which is electrically heated to a constant temperature, whereas the white squares are made out of plastic. The pattern used for calibration is shown in Figure 7.

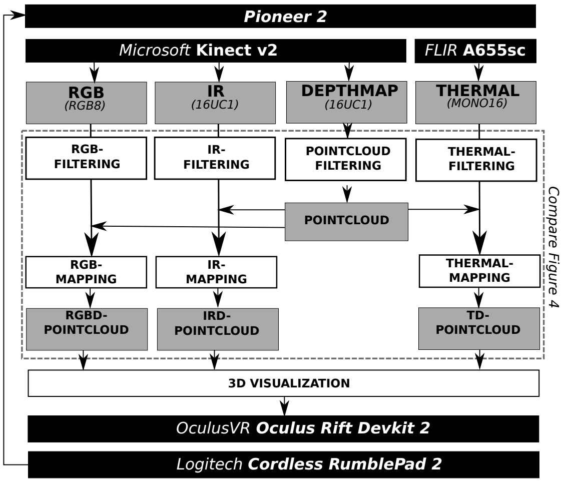

Figure 6: Overview of the input and output structure.

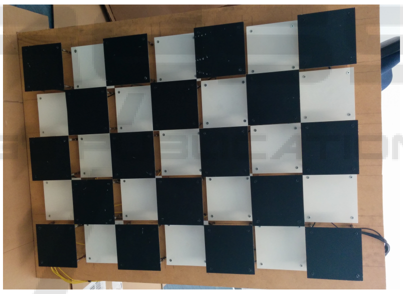

Figure 7: A three-dimensional, heated calibration pattern for thermo-depth calibration.

Besides the differences in temperature, the black and white chessboard squares also differ in depth. Because the depth image also provides intensity images (active IR), the depth differences were not used for depth camera calibration. The size of one square is 100 mm x 100 mm with a depth difference between a black and a white square of 40 mm.

4.3 Mapping

The results of the mapping process are shown in Figure 8(a) to 8(l).

The first image of every row shows the raw, unregistered point cloud which is generated according to Section 3.4. The following figures are showing the point cloud registered to RGB, active IR and thermal

[1] https://github.com/ros-visualization/oculus_ rviz_ plugins, June 2015

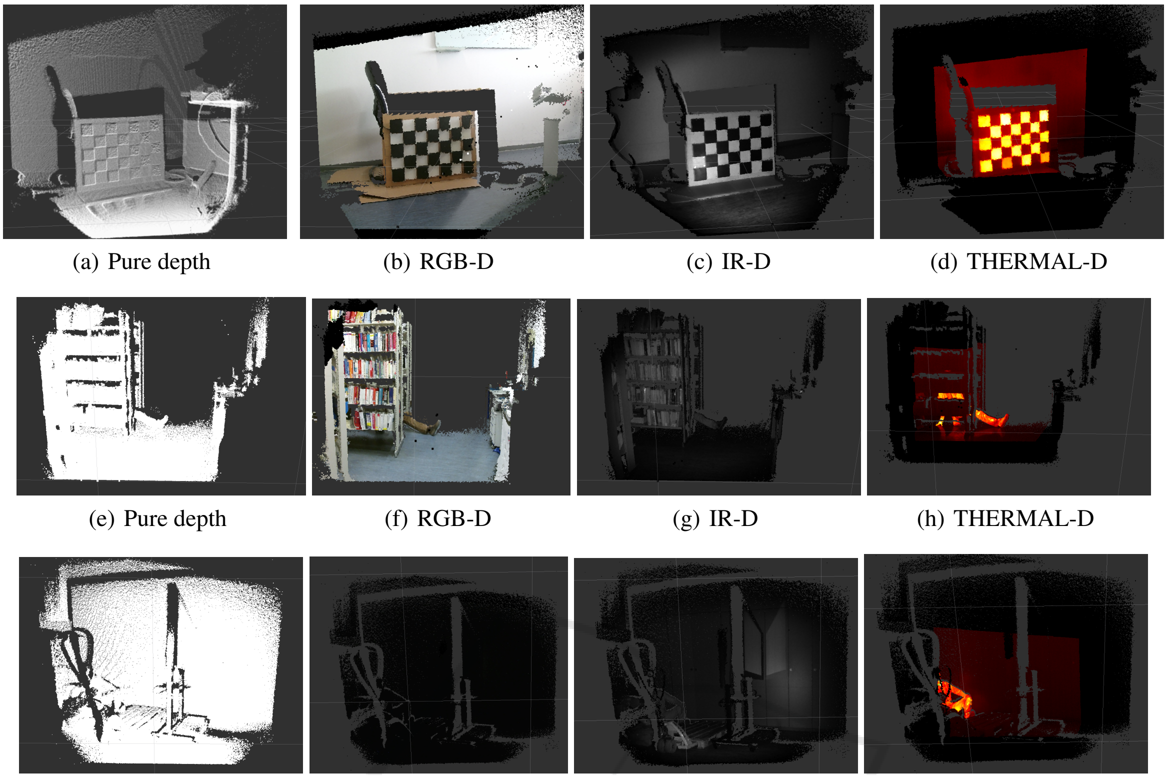

(a) Pure depth (b) RGB-D (c) IR-D (d) THERMAL-D

(e) Pure depth (f) RGB-D (g) IR-D (h) THERMAL-D

(i) Pure depth (j) RGB-D (k) IR-D (l) THERMAL-D

Figure 8: Final mapping results for different scenes: (a) to (d) Different image sources mapped onto the calibration pattern (e) to (f) Person hidden behind a bookshelf, (g) to (h) Person lying in the edge of a dark storage room.

images. To illustrate the advantages of the different sensors, each row shows a different scenario:

Figure 8(h) shows uncolored, black points in the outer region of the point cloud caused by varying field of views of the depth and the thermal camera. Because the thermal camera has a smaller vertical and horizontal field of view, the thermal image provides no information which could be mapped to the outer points of the point cloud. Because of the high number of points, surfaces and small details can be recognized.

5 RESULTS

The following section evaluates the results of the presented approach regarding calibration quality and processing time.

5.1 Calibration

The cameras have been calibrated using the calibration pattern described in Section 4.2. For calibration, 40 images have been made from different poses around the calibration pattern with every camera. The results of the intrinsic calibrations are shown in Table 1. The distortion parameters for lens distortion removal are not listed in Table 1.

The quality of the calibration can be evaluated based on the resulting root mean square reprojection error (rms), which is calculated for the images made after applying the intrinsic calibration. Based on the total pattern size of 700 *mm* x 500 *mm*, the pattern was unsuited to be placed in the near field in front of the camera depending on the camera's field of view which affects the quality of the calibration.

The calibration of the IR camera got a higher rms compared to the RGB calibration, probably because the chessboard points could not be reliably detected in the whole field of view due to the limited IR lightning in the outer regions of the image. Additionally, the IR image is stronger affected by image noise compared to the RGB image. Furthermore, the resolution of the IR camera is smaller than the resolution of the RGB camera which reduces the accuracy of the detected points.

The rms of the thermal camera is higher than the

Table 1: Results of the intrinsic calibration (without distortion parameters).

Camera	$\mathbf{f_x}$[px]	$\mathbf{f_y}$[px]	$\mathbf{c_x}$[px]	$\mathbf{c_y}$[px]	**rms**
RGB	1.063e+03	1.066e+03	9.59e+02	5.541e+02	0.1734
IR and Depth	3.633e+02	3.631e+02	2.442e+02	2.030e+02	0.6856
Thermal	7.984e+02	7.997e+02	3.140e+02	2.371e+02	1.0351

rms of the RGB and the IR camera. This may be caused by the fixed focus which has been used for calibration, providing a lower range where objects are in focus compared to the IR camera. This leads to blur and consequently to inaccuracy detecting the chessboard points. The results of the extrinsic calibration regarding the rms are presented in Table 2.

Based on the results of the mapping, the rms of the extrinsic calibration can be considered as sufficient for visualization.

5.2 Processing Time

To avoid simulator sickness and to enable the operator to react fast on occurring events, all delays have to be kept as small as possible. Therefore, the presented algorithm has been implemented using Compute Unified Device Architecture (CUDA) to operate on a NVIDIA GTX 970 GPU with 1664 cores. The CUDA-based GPU implementation is compared with a single core CPU implementation. Table 3 gives an overview of the average processing time of $10,000$ frames for the presented algorithm performed on the CPU and the GPU. The processing time on the GPU has been measured using the CUDA event API; the processing time of the CPU version has been measured using clock ticks elapsed since the algorithm has been started divided by the clocks per second.

The highest acceleration could be archived by implementing the preprocessing step on the GPU (which includes bilateral filtering and flying pixel detection as described in Section 3.1). The preprocessing step could be accelerated by $112,43$ *ms* which is an acceleration of 85.37 % referred to the former duration which makes 97.88 % of the total acceleration.

Using the GPU implementation, the complete mapping process could be accelerated by 80.03 % compared to the CPU implementation which is an acceleration of 114.73 *ms*. While the processing rate of the CPU implementation limits the possible frame rate to 7 fps, the GPU implementation allows a frame rate of 35.59 fps. Because the frame rate is limited to 30 fps by the depth camera, the new processing time of 28.84 *ms* can be considered to be sufficient. To perform the mapping on the GPU, all necessary data need to be copied to the GPU memory for processing. After processing has been completed, the data need to be copied back to be accessible by the CPU. The time needed for allocation, deallocation and copying has been pooled as *Memory Operations* in Table 3.

5.3 Limitations

Like all ToF cameras, the *Kinect v2* can be affected by direct sunlight outshining the light emitted by the ToF camera. To evaluate the performance of the presented approach, the setup has been tested indoor in a controlled environment. For this reason the approach presented in this paper is limited to applications with no direct sunlight. There are, however, ToF cameras available with additional light sources which are confirmed to be suited for outdoor application as the OI-VS-1000 produced by ODOS Imaging.

6 CONCLUSION AND FURTHER WORK

In this paper, a new VR control concept for operating robots in SAR scenarios has been introduced. The presented approach intuitively visualizes different sensor signals as RGB, thermal or infrared images by merging them with 3D data generated by a ToF-based depth camera. The three-dimensional point cloud is then visualized on a tracked head-mounted display to provide the additional information. The approach has been evaluated under laboratory conditions using a Pioneer 2 mobile robot equipped with a depth, RGB, IR and thermal camera.

For intrinsic and extrinsic calibration, a new calibration pattern has been introduced. It has been shown, that the presented calibration pattern is well suited for multi-sensor calibration with acceptable root mean square reprojection errors.

To avoid simulator sickness and decrease the reaction time of the operator, the multi-sensor mapping has been performed on a GPU. It has been shown, that performing the mapping on the GPU can significantly decrease the processing time by about 80 % compared to traditional CPU implementation consequently decreasing the delay. It must be taken into account, that the GPU version had been compared against a single threaded CPU implementation. The relative accelera-

Table 2: Results of the extrinsic calibration.

Transformation	**rms**
RGB - Depth	0.323
Thermal - Depth	1.019

Table 3: Comparison between the processing time performing the mapping for one image as CPU and GPU implementation. Average value of 10,000 processing steps with a depth image resolution of 512*x*424.

Step	**Average Time CPU** [ms]	**Percentage of Total** [%]	**Average Time GPU** [ms]	**Percentage of Total** [%]	**Acceleration** [%]
Preprocessing	131.69	92.20	19.26	68.54	85.37
Point Cloud Generation	4.07	2.8	3.16	8.89	22.36
Transformation	1.13	0.79	0.60	2.10	46.90
Image Plane Projection	4.80	3.34	3.22	8.73	32.92
Inverse Transformation	1.14	0.79	0.60	2.10	47.37
Memory Operations	-	-	1.26	4.5	-
Total	**142.83**	**100**	**28.1**	**100**	80.03

tion of the GPU implementation would decrease compared against a fully optimized, multi-threaded CPU version of the mapping procedure. To verify the expected reduction of simulator sickness and resultant fatigue, additional experiments in real-life conditions still need to be performed.

The presented approach has been evaluated in a lab scenario. To prove the effectiveness of the new control approach compared to traditional control concepts, the system needs to be evaluated in real SAR scenarios.

The overview of the surrounding structures can be further improved by building an environmental map registering the multichannel scans. For such applications, the multichannel point cloud can be used to increase the robustness of correspondence identification for scan registration to avoid ambiguity in scan images.

To increase the quality for the intrinsic and extrinsic calibration, the field size of the calibration pattern could be reduced to be able to calibrate the camera in the near region. It should be examined, whether haptic feedback would lead to a further improvement regarding the usability aspects for untrained operators. Moreover, the mapped sensor data could be used to improve information models as presented in (Gernert et al., 2014) with additional information layers. The mapping of thermal images onto three-dimensional structures is useful for improved temperature estimation as presented in (Zeise et al., 2015).

REFERENCES

Brown, D. C. (1971). Close-range camera calibration. In *Photogrammetric Engineering*, volume 37, pages 855–866.

Cui, J., Tosunoglu, S., Roberts, R., Moore, C., and Repperger, W. (2003). A review of teleoperation system control. In *Florida Conference on Recent Advances in Robotics (FCRAR)*, pages 1–12, Boca Raton, FL, USA.

Endres, F., Hess, J., Sturm, J., Cremers, D., and Burgard, W. (2013). 3D mapping with an RGB-D camera. volume 30, pages 177–187.

Gernert, B., Schildt, S., L.Wolf, Zeise, B., Fritsche, P., Wagner, B., M.Fiosins, Manesh, R., and Mueller, J. (2014). An interdisciplinary approach to autonomous team-based exploration in disaster scenarios. In *IEEE International Symposium on Safety, Security, and Rescue Robotics (SSRR)*, pages 1–8, Hokkaido, Japan.

Hainsworth, D. W. (2001). Teleoperation user interfaces for mining robotics. In *Autonomous Robots*, volume 11, pages 19–28, Hingham, MA, USA.

Henry, P., Krainin, M., Herbst, E., Ren, X., and Fox, D. (2010). RGB-D mapping: Using depth cameras for dense 3d modeling of indoor environments. In *RGB-D: Advanced Reasoning with Depth Cameras Workshop in conjunction with RSS*, Zaragoza, Spain.

Izadi, S., Kim, D., Hilliges, O., Molyneaux, D., Newcombe, R., Kohli, P., Shotton, J., Hodges, S., Freeman, D., Davison, A., and Fitzgibbon, A. (2011). Kinectfusion: Real-time 3d reconstruction and interaction using a moving depth camera. In *ACM Symposium on User Interface Software and Technology*, pages 559–268, Santa Barbara, CA, USA.

LaValle, S. M., Yershova, A., Katsev, M., and Antonov, M. (2014). Head tracking for the oculus rift. In *IEEE International Conference on Robotics and Automation (ICRA)*, pages 187 – 194, Hong Kong, China.

Moghadam, P. and Vidas, S. (2014). Heatwave: The next generation of thermography devices. In *International Society for Optical Engineering (SPIE)*, volume 9105, page 91050.

Nguyen, L., Bualat, M., Edwards, L., Flueckiger, L., Neveu, C., Schwehr, K., Wagner, M., and Zbinden, E. (2001). Virtual reality interfaces for visualization and control of remote vehicles. *Autonomous Robots*, 11(1):59–68.

Okura, F., Ueda, Y., Sato, T., and Yokoya, N. (2013). Teleoperation of mobile robots by generating augmented free-viewpoint images. In *IEEE and RSJ International Conference on Intelligent Robots and Systems (IROS)*, pages 665–671, Tokyo, Japan.

Ridao, P., Carreras, M., Hernandez, E., and Palomeras, N. (2007). Underwater telerobotics for collaborative research. In Ferre, M., Buss, M., Aracil, R., Melchiorri, C., and Balaguer, C., editors, *Advances in Telerobotics*, volume 31 of *Springer Tracts in Advanced Robotics*, pages 347–359. Springer Berlin Heidelberg.

Saitoh, K., Machida, T., Kiyokawa, K., and Takemura, H. (2006). A 2D-3D integrated interface for mobile robot control using omnidirectional images and 3d geometric models. In *IEEE and ACM International Symposium on Mixed and Augmented Reality (ISMAR)*, pages 173–176, Washington, DC, USA.

Stoll, E., Wilde, M., and Pong, C. (2009). Using virtual reality for human-assisted in-space robotic assembly. In *World Congress on Engineering and Computer Science*, volume 2, San Francisco, USA.

Tomasi, C. and Manduchi, R. (1998). Bilateral filtering for gray and color images. In *IEEE International Conference on Computer Vision (ICCV)*, pages 839–846, Washington, DC, USA.

Vidas, S. and Moghadam, P. (2013). Heatwave: A handheld 3D thermography system for energy auditing. In *Energy and Buildings*, volume 66, pages 445 – 460.

Vidas, S., Moghadam, P., and Bosse, M. (2013). 3D thermal mapping of building interiors using an RGB-D and thermal camera. In *IEEE International Conference on Robotics and Automation (ICRA)*, pages 2311–2318, Karlsruhe, Germany.

Yong, L. S., Yang, W. H., and Jr, M. A. (1998). Robot task execution with telepresence using virtual reality technology. In *International Conference on Mechatronic Technology*, Hsinchu, Taiwan.

Zeise, B., Kleinschmidt, S. P., and B.Wagner (2015). Improving the interpretation of thermal images with the aid of emissivity's angular dependency. In *IEEE International Symposium on Safety, Security, and Rescue Robotics (SSRR)*, pages 1–8, West Lafayette, Indiana, USA.

Zhang, Z. (1999). Flexible camera calibration by viewing a plane from unknown orientations. In *IEEE International Conference on Computer Vision*, volume 1, pages 666–673, Kerkyra, Greece.

Zhang, Z. (2000). A flexible new technique for camera calibration. In *IEEE Transactions on Pattern Analysis and Machine Intelligence*, volume 22, pages 1330–1334.